White Rose Research Online

eprints@whiterose.ac.uk
https://eprints.whiterose.ac.uk
Universities of Leeds, Sheffield and York

Deposited via The University of Sheffield.

White Rose Research Online URL for this paper:
https://eprints.whiterose.ac.uk/id/eprint/86360/

Version: Accepted Version

Article:
Walther, T. (2015) Accurate measurement of atomic segregation to grain boundaries or to planar faults by analytical transmission electron microscopy. Physica Status Solidi (c), 12 (3). 310 - 313. ISSN: 1862-6351

https://doi.org/10.1002/pssc.201400121

Reuse
Items deposited in White Rose Research Online are protected by copyright, with all rights reserved unless indicated otherwise. They may be downloaded and/or printed for private study, or other acts as permitted by national copyright laws. The publisher or other rights holders may allow further reproduction and re-use of the full text version. This is indicated by the licence information on the White Rose Research Online record for the item.

Takedown
If you consider content in White Rose Research Online to be in breach of UK law, please notify us by emailing eprints@whiterose.ac.uk including the URL of the record and the reason for the withdrawal request.

pss-Header will be provided by the publisher

Accurate measurement of atomic segregation to grain boundaries or to planar faults by analytical transmission electron microscopy

Thomas Walther*

Kroto Centre for High-Resolution Imaging & Analysis, Department of Electronic & Electrical Engineering, University of Sheffield, Mappin Street, Sheffield, S1 3JD, England, UK

Received ZZZ, revised 8 December 2014, accepted 5 January 2015
Published online ZZZ (Dates will be provided by the publisher.)

Keywords: Analytical electron microscopy, (scanning) transmission electron microscopy, segregation, X-ray mapping.

* Corresponding author: e-mail t.walther@sheffield.ac.uk, Phone: +44 114 222 5891, Fax: +44 114 222 5143

A method of analytical transmission electron microscopy is described that has been successfully applied to study dopant segregation to inversion domain boundaries in zinc oxide, to quantify the thicknesses of sub-nanometre thin epitaxial layers grown by molecular beam epitaxy of indium arsenide (InAs) on gallium arsenide (GaAs) or silicon/germanium on silicon and proved the absence of any gettering of As or Ga dopants at Sigma=3 {111} grain boundaries in silicon, with a precision of <1 atom/nm^2 in each case. Here, the case study of InAs/GaAs is reviewed in detail and the procedure for quantification of full hyperspectral data sets is explained.

Copyright line will be provided by the publisher

1 Introduction Transmission Electron Microscopy (TEM) is routinely used to measure the width of thin layers in cross-sectional geometry, down to single atomic planes, and, in scanning mode (STEM) combined with add-on detectors for spectroscopy of either the electron energy-loss (EELS) or the characteristic X-ray lines (energy-dispersive X-ray spectroscopy, EDXS), to measure the chemical composition. A major problem with quantification is encountered if such layers are thinner than typical unit cell dimensions of crystals (typically, 0.3-0.5nm). This is due to the general inability to reliably measure the fractional occupancies of atomic columns imaged in projection in almost all cases. Also, the effect that even moderate broadening of the electron beam has while it transverses the material, which is due to multiple elastic/inelastic scattering, can falsify the apparent chemical concentration a lot. Multi-slice calculations have been performed using the Semper software package [1]. The approach is based on an incremental increase of the electron beam size to describe the broadening of an initial top-hat profile as the beam transverses, atomic layer by atomic layer, a model crystal of a given thickness t with a single monolayer of different chemical composition embedded, parallel to and in the middle of the electron beam. The beam broadening is assumed proportional to $t^{1.5}$ as in most models. More details are supplied in ref. [2].

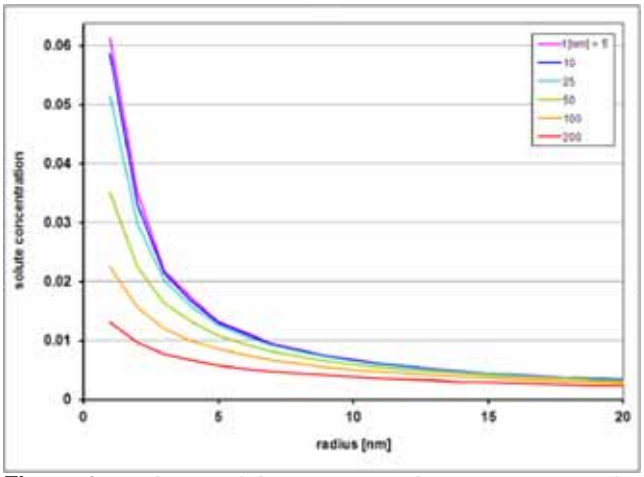

Figure 1 Simulation of the apparent solute concentration for a planar fault 0.2 nm wide and covered to 50 % by a solute element, for a matrix similar to silicon (Z=14) imaged at 100 kV, X-ray detection from the complete hemisphere above the fault, beam diameters from 2 to 40 nm and various specimen thicknesses t [3].

Copyright line will be provided by the publisher

Figure 1 demonstrates that if a single lattice plane in a crystal with a simple cubic lattice (a=0.4nm) is filled to 50% with some segregated dopant atoms and imaged edge-on by a 100kV electron beam of 1nm radius or bigger, the apparent solute concentration will be ≤6% even in the most favourable cases, i.e. systematically wrong by about an order of magnitude.

While this could in principle be accounted for by explicit reverse modelling, the effect will be a pronounced function of specimen thickness that leads to beam broadening, and numerical results for small electron probes will be prone to large relative errors. In a recent publication [3] we have summarised the present state of analytical microscopy studies of planar faults and grain boundaries and explained why aberration correction in electron microscopy can produce better images and improved spectra but cannot solve this basic quantification issue, which is due to a combination of several factors, amongst which are statistical issues related to small probed volumina [4], increased beam damage induced by electron probes with higher current densities [5] and an interplay between channelling effects and beam spread [6-8]. Therefore, new ways to quantify analytical spectra (EELS or EDXS) are required.

Here, one such unified approach to analyse series of spectra is described, which can be applied to either EEL or EDX spectra acquired in either nano-probe TEM mode or in STEM mapping mode, some of which have already been employed successfully in a number of cases [9].

2 Simulations and detection principles

2.1 Simulations If one plots the reverse of the solute concentration, i.e. the matrix/solute ratio, then this depends linearly on the size of the electron probe used for analysis, as long as the latter is >1nm and the sample not excessively thick. This is demonstrated in Figure 2. In [2] the following analytical expression for the relationship between the matrix/solute ratio, R, the solute concentration in the matrix (solubility), x, the beam radius, r, and the effective chemical width of the fault, d, defined as the product of geometrical width and fractional occupancy, has been derived from simple geometrical considerations:

$$R = \frac{(1-x)(\pi r^2 - 2rd)}{x\pi r^2 + 2rd} \approx \frac{\pi r}{2d} - 1 \quad \text{for small } x \qquad (1)$$

so that a plot of $R(r)$ has slope $\pi/(2d)$ and thus d can be determined by linear regression. The simulations in [2] showed that for various imaging and materials parameters there was a general trend that the more linear the plots of $R(r)$ were, the less the numerical results deviated from the nominal input values.

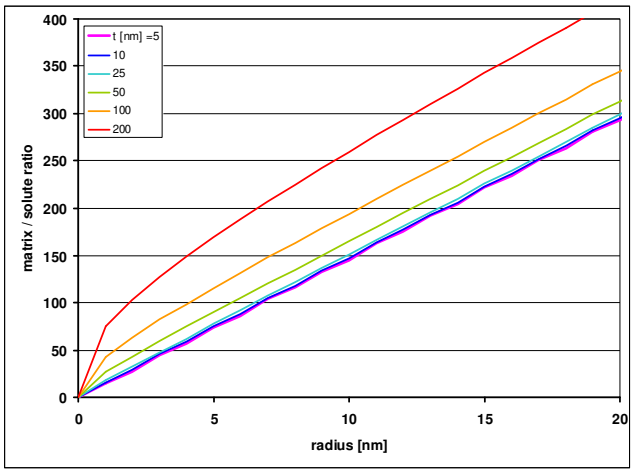

Figure 2 Same simulation as for Figure 1, now plotting the reverse of solute concentration [3].

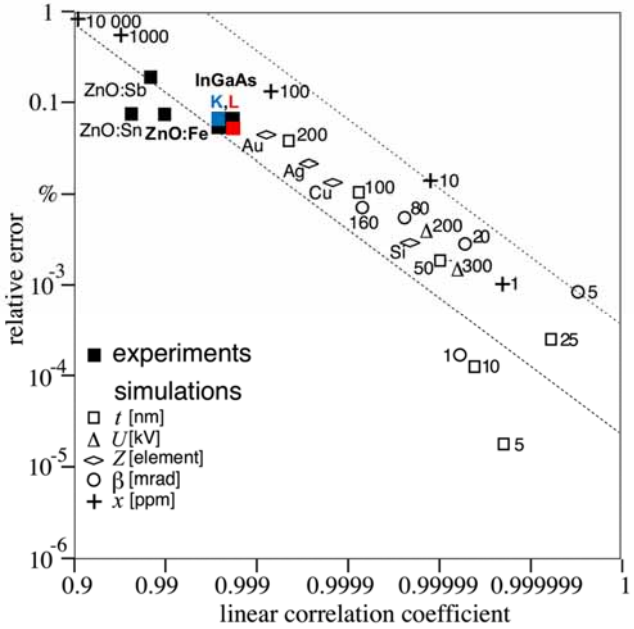

Figure 3 Scatter graph of relative errors from simulations for various conditions vs. linearity of the plots of $R(r)$ [2], along with data points from experiments for ZnO [10-12] and InGaAs [13], the latter presented seperately for K & L lines in Figure 6.

Experiments conducted on inversion domain boundaries in zinc oxide doped with Sb^{V+} [10], Sn^{IV+} [11] or Fe^{III+} [12] ions lay quite close to the rather narrow corridor expected from simulations, as indicated by dashed lines in Figure 3.

2.2 Detection principles It has been recognised early [14] that the proposed technique does not necessarily rely on round electron probes produced in nano-beam mode, with quasi-parallel or only slightly focused TEM illumination, as modelled in [2]. It can also be adopted to STEM mode, whereby the set of measurements with concentric round areas is replaced with a square area that is

Copyright line will be provided by the publisher

raster scanned by a strongly focused electron probe. If a full set of hyperspectral data is acquired, elemental maps can be extracted for each rectangular sub-region of the full scan, as function of the scan length, *L*, perpendicular to the interface or fault. As demonstrated in the sketch of Figure 4, this effectively replaces round regions of diameter $2r$ (area πr^2) by squares of length L (area L^2), so equation (1) becomes

$$R = \frac{(1-x)(L^2-Ld)}{xL^2+Ld} \approx \frac{L}{d} - 1 \qquad \text{for small } x \qquad (2)$$

Finally, it is noted that the scanned regions need not be squares but can extend parallel to the fault as long as is necessary, as due to the symmetry of the problem the matrix/solute ratio does not change along the fault.

Figure 4 compares sketches for TEM and STEM geometry. While references [9-11] used the nano-probe probe set-up sketched in Figure 4a, the results shown below for InGaAs have been acquired in STEM mapping mode, similar to the sketch in Figure 4c.

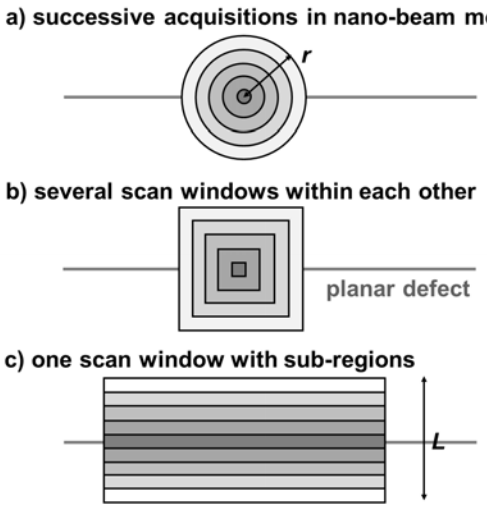

Figure 4 Sketch of several possible implementation geometries

3 Experimental Results A sample of three In(Ga)As quantum wells (QWs) have been grown by molecular beam epitaxy, with increasing nominal thickness, from just below to just above the critical InAs thickness for the Stranksi-Krastanow transition from flat (two-dimensional) to rough (three-dimensional) growth. Cross-sectional analysis by STEM has been performed by X-ray mapping in a JEOL 2010F field-emission microscope equipped with an analogue scan unit and an Oxford Instruments ultra-thin window Si:Li Xray detector. While the electron probe size was ~1nm, the sampling of 2.2nm/pixel and the off-zone axis tilt to avoid channelling conditions mean that the layers which are around a single unit cell (2 monolayers of the group-III sub-lattice, ~0.56nm) wide, will appear broadened to ~6nm. More details of the growth and STEM investigation are described in [13]. The point relevant to this study is that the X-ray maps displayed below in Figure 5 have been recorded with the Oxford Instruments ISIS300 v.3.2 software which has issues in, firstly, subtracting the non-specific background under the characteristic X-ray lines as the output are images in tiff-format which simply integrate X-ray intensities around characteristic X-ray lines and, secondly, ignore the *k*-factors. To get improved reliability, maps of elements not present within the specimen were also acquired so that the background under the L-edges could at least be estimated by linear extrapolation and subtracted. Also, we have used improved *k*-factors obtained by fitting the thickness dependence of apparent Ga/As and In/As X-ray intensities from cleaved GaAs and InAs wedge samples [15]. For our new aberration corrected 300kV instrument we are now using a much improved approach that relies on hyperspectral imaging, acquiring sets of X-ray and electron energy-loss spectra point-by-point and storing the whole multi-dimensional data cube, with individual spectra for each point in the map. Such a procedure is now available on almost all modern systems. In this way, the complete background fitting and subtraction procedures for spectroscopy can be used for each point or sub-region in the map, thereby improving the accuracy of extracting net intensities in EDXS and/or EELS [12,16] beyond that which has been possible here in Figure 5 where only simple window integration and linear background estimates have been applied. The systematic errors of the new approach will then be reduced simply to the relative uncertainties in the ratios of the *k*-factors (which determines the scale of the *y*-axis in Figure 2) and of the magnification (which determines the scale of the *x*-axis in Figure 2). The statistical errors are taken into account by the linear regression fitting where Figure 3 indicates that R^2 will provide an independent measure of the expected precision.

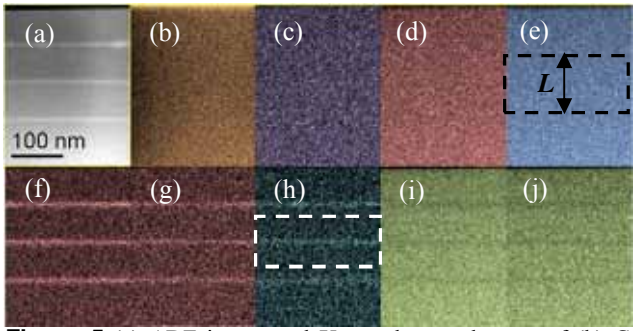

Figure 5 (a) ADF image and X-ray elemental maps of (b) C_K (26-184 counts), (c) background of S_K (0-29 counts), (d) As_L (30-205 counts), (e) As_K (29-240 counts), (f) $In_{L\alpha}$ (1-33 counts), (g) $In_{L\beta}$ (0-29 counts), (h) $In_{K\alpha}$ (0-20 counts), (i) Ga_L (50-336 counts) and (j) Ga_K (32-246 counts). A suitable window of height *L* around the middle quantum well is sketched for As_K and $In_{K\alpha}$. The counts state minima and maxima of the net signals of the X-ray maps after background subtraction.

Copyright line will be provided by the publisher

While the group-V sub-lattice in InGaAs is occupied only by As atoms, which may thus be considered to constitute half of the matrix atoms in the above model, the group-III sub-lattice is made up of Ga atoms and some In atoms (at the position of the quantum wells). Hence, the As/In ratio corresponds to the matrix/solute ratio in our model, and a plot of its slope vs. the height of the integration window, L, will yield the total effective chemical width of the layers as the inverse of the slope. These values in nm can be converted to multiples of group-III monolayers (0.28nm) and can be evaluated for each quantum well individually from various line ratios (As_L/In_L, As_K/In_K, As_L/In_K, As_K/In_L, $(Ga_L+In_L)/In_L$ and equivalent combinations). Results from As_K/In_K and As_L/In_L are plotted in Figure 6 and the numerical results from evaluating the slopes of these plots are tabulated in Table 1. As can be seen, the error bars from slope fitting are small, and the difference between results from K and L line quantification for the two first grown quantum wells (QW 1 & 2) differ by more than the expected statistical errors, which can be explained by these regions being further away from the specimen edge, hence a bit thicker so that softer X-ray lines will get more strongly absorbed. The scatter of all values around, on the average, 1.67±0.17 monolayers is in good agreement with the value from reflection high-energy electron diffraction of the surface evolution during growth and also with published data for the Stranski-Krastanow growth transition for InAs/GaAs of 1.8 monolayers [17, 18].

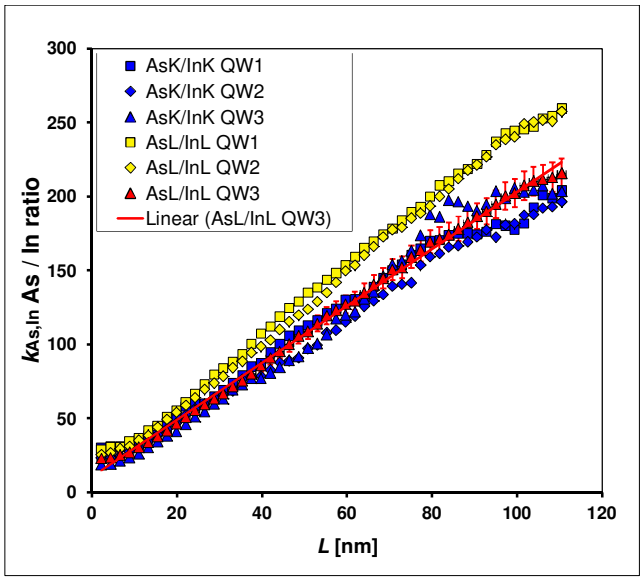

Figure 6 Plot of k-factor corrected As/In ratios as function of the window size, L, for integration of the map intensities around the In(Ga)As layers [13]. The intensities of the K lines were integrated from the blue maps, and the intensities of the L lines from the red coloured maps in Figure 5, where rectangular regions of height L were chosen around each quantum well as indicated, extending up to 60nm either side so signals from adjacent quantum wells (80nm apart) did not 'leak' in significantly. For the As L/ In L plot of QW3 (red triangles) error bars from counting statistics and the k-factor uncertainty remaining after re-calibration [15] are included, along with the linear fit (red line).

Table 1 effective InAs monolayers, determined from slope fit

X-ray lines used	QW 1	QW 2	QW 3
K	1.77±0.13	1.90±0.11	1.67±0.13
L	1.46±0.07	1.48±0.05	1.76±0.07

* QW 1 is the lowest quantum well, QW 3 the top one. All values are in equivalents of full InAs group-III monolayers (full monolayer=0.28nm).

4 Conclusion A method to quantify the amount of solute atoms segregated to a planar fault or a grain boundary, or, more generally, the average effective chemical width of any straight planar defect in a crystalline solid, has been developed. This was originally implemented in nano-beam TEM mode [2,3], then it was shown that X-ray mapping in STEM mode as applied here can give the same result [13,14], and an improved procedure to obtain such information from full hyperspectral data sets from any chemical spectroscopic imaging method has been outlined in this article. It is hoped that in the future both EDXS and EELS data acquired in STEM can thus be more reliably quantified and correlated to determine the effective chemical width of thin layers which will aid an understanding of their complete microstructural, crystallographic, compositional and electronic properties.

Acknowledgements The author would like to thank the crystal growers Mark Hopkinson, Nina Daneu, Aleksander Recnik and Yutaka Ohno for provision of specimen material and A. Recnik for help in developing the original technique as sketched in Figure 3a.

References

[1] W.O. Saxton, T.J Pitt and M. Horner, Ultramicroscopy **4**, 343 (1979).
[2] T. Walther, J. Microsc. **215**, 191 (2004).
[3] T. Walther, M. Hopkinson, N. Daneu, A. Recnik, Y. Ohno, K. Inoue and I. Yonenaga, J. Mater. Science **49**, 3898 (2014).
[4] H Müllejans, Z. Metallkunde **94**, 298 (2003).
[5] R.F. Egerton, P. Li and M. Malac, Micron **35**, 399 (2004).
[6] A. Howie, Philos. Mag. **14**, 223 (1966).
[7] L. Reimer, H. Gilde and K.H. Sommer, Optik **30**, 590 (1970).
[8] D.B. Williams, J.R Michael, H.I. Goldstein and A.D Romig, Ultramicroscopy **47**, 121 (1992).
[9] T. Walther, A. Recnik and N. Daneu, Microchim. Acta **155**, 313 (2006).
[10] A. Recnik, N. Daneu, T. Walther and W. Mader, J. Am. Ceram. Soc. **84**, 2657 (2001).
[11] N. Daneu, A. Recnik, T. Walther and W. Mader, Proc. MC2003, Dresden, Germany (Cambridge University Press, Cambridge) Microsc. Microanal. **9**, Suppl. 3, 286 (2003).

Copyright line will be provided by the publisher

[12] T. Walther, F. Wolf, A. Recnik and W. Mader, Int. J. Mater. Res. **97**, 934 (2006).
[13] T. Walther and M. Hopkinson, Proc. 18th Intern. Conf. on Microscopy of Semiconducting Materials, Oxford, UK (IoP Publishing, Bristol) J. Phys. Conf. Ser. **209**, 012035 (2010).
[14] T. Walther, J. Microsc. **223**, 165 (2006).
[15] T. Walther, Proc. Electron Microsc. And Analysis Group Conf., Sheffield, UK (IoP Publishing, Bristol) J. Phys. Conf. Ser. **241**, 012016 (2010).
[16] B.G. Mendis, M. MacKenzie and A.J. Craven, Ultramicroscopy **110**, 105 (2010).
[17] D. Leonhard, K. Pond and P.M. Petroff, Phys. Rev. B **50**, 11687 (1994).
[18] Y. Nabetani, N. Yamamoto, T. Tokuda and A. Sasaki, J. Crystal Growth **146**, 363 (1995).

Copyright line will be provided by the publisher